Article:
Jovanovic, V.D., Hofling, S., Indjin, D. et al. (5 more authors) (2006) Influence of doping density on electron dynamics in GaAs/AlGaAs quantum cascade lasers. Journal of Applied Physics, 99 (10). 103106-(9 pages). ISSN 1089-7550

https://doi.org/10.1063/1.2194312

Influence of doping density on electron dynamics in GaAs/AlGaAs quantum cascade lasers

V. D. Jovanović[a)]
School of Electronic and Electrical Engineering, University of Leeds, Leeds LS2 9JT, United Kingdom

S. Höfling
Technische Physik, Universität Würzburg, Würzburg, Am Hubland D-97080, Germany

D. Indjin, N. Vukmirović, Z. Ikonić, and P. Harrison
School of Electronic and Electrical Engineering, University of Leeds, Leeds LS2 9JT, United Kingdom

J. P. Reithmaier[b)] and A. Forchel
Technische Physik, Universität Würzburg, Würzburg, Am Hubland D-97080, Germany

(Received 23 October 2005; accepted 23 February 2006; published online 31 May 2006)

A detailed theoretical and experimental study of the influence of injector doping on the output characteristics and electron heating in midinfrared GaAs/AlGaAs quantum cascade lasers is presented. The employed theoretical model of electron transport was based on a fully nonequilibrium self-consistent Schrödinger-Poisson analysis of the scattering rate and energy balance equations. Three different devices with injector sheet doping densities in the range of $(4-6.5)\times 10^{11}$ cm^{-2} have been grown and experimentally characterized. Optimized arsenic fluxes were used for the growth, resulting in high-quality layers with smooth surfaces and low defect densities. A quasilinear increase of the threshold current with sheet injector doping has been observed both theoretically and experimentally. The experimental and calculated current-voltage characteristics are in a very good agreement. A decrease of the calculated coupling constant of average electron temperature versus the pumping current with doping level was found. © *2006 American Institute of Physics*. [DOI: 10.1063/1.2194312]

I. INTRODUCTION

The idea of electrically pumped intersubband lasers or quantum cascade lasers (QCLs) as unipolar semiconductor devices utilizing intersubband transitions in a repetition of identical coupled multi-quantum-well structures was pioneered by Kazarinov and Suris.[1] However, more than 20 years passed until the experimental realization was demonstrated by Faist *et al.* at Bell Laboratories on an InP substrate.[2] Since then tremendous progress in QCL research has resulted in bidirectional,[3] multiwavelength,[3,4] ultrabroadband,[5] above room temperature continuous-wave (cw) operation,[6–8] sum-frequency and higher order harmonic generation,[9–11] and fully integrated electrically pumped Raman lasers.[12] Moreover, laser operation has been reported on other material systems, i.e., AlGaAs on a GaAs substrate[13] and Al(Ga)Sb on InAs.[14] Devices with Sb-containing barriers on both InAs substrate[14–16] as well as on InP substrate[17–19] are promising for either increasing the electron confinement or reducing the emission wavelength, and above room temperature pulsed operation on both substrates was recently reported.[16,18]

Since the realization[13] of the GaAs-based quantum cascade laser, an impressive extension of the attainable infrared frequency range has been achieved and can be operated at wavelengths as long as 160 μm.[20] The design of QCLs based on GaAs/AlGaAs can be made very flexible by varying the Al content due to naturally occurring near lattice matched material system across the full range of Al contents. Hence, following the first terahertz QCL,[21] several laser designs based on 15% Al content in the barriers were presented, approaching high temperature pulsed operation[22] (137 K) and above[23] or close to[24] liquid nitrogen temperature cw operation.

GaAs-based QCLs emitting in the midinfrared spectral region have so far used Al contents of 33%,[13,25] 45%,[26–28] and 100%,[29–31] respectively. Pulsed room temperature operation has been reported only for designs with 45% Al content[26–28] except for one design employing AlAs barriers and monolayers of InAs deposited at the antinode of the electron wave functions in order to improve the electron confinement.[30] Achieving cw operation in midinfrared GaAs-based QCLs is a very challenging task due to the relatively high threshold current densities. Nevertheless, cw operation has been reported[29,32,33] with operating temperatures up to 150 K.[33]

However, the output characteristics of midinfrared GaAs-based devices are still rather poor in comparison to InP-based midinfrared QCLs, which can lase in cw regime at room temperature.[6] For further improvements, a detailed knowledge of crucial design parameters as well as an understanding of relevant physical limitations of particular designs and further investigation of the influences of relevant physi-

[a)]Present address: Lehman Brothers, 25 Bank Street, London E14 5LE, United Kingdom; electronic mail: eenvj@leeds.ac.uk
[b)]Present address: Technische Physik, Insititute for Nanostructure Technologies and Analytics, University of Kassel, Heinrich-Plett-Strasse 40, D-34132 Kassel, Germany.

cal and technological parameters are highly desirable. Together with experimental investigations, a systematic and compact theoretical modeling is a necessary step towards improvements of the existing structures and the understanding of physical processes within. These include Monte Carlo simulation,[34–37] nonequilibrium Green's function formalism,[38,39] as well as self-consistent rate equations model.[40,41]

The doping level in the active region is an important parameter with particular influence on the dynamic working range of QCLs. Until now, very few experimental investigations have been presented including the influence of the injector doping on InP-based[42–44] and GaAs-based[45–48] QCL threshold currents.

Due to the superior device performance of midinfrared devices with 45% Al content there is a demand for a comprehensive experimental and theoretical analysis of these designs. In this work, we report such an investigation of three-quantum-well design[26] in which the influence of the injector doping density on the carrier dynamics is analyzed.

II. THE QCL MODEL

Electron transport in QCLs was simulated within the framework of a fully self-consistent scattering theory approach.[40,41] For that purpose, the QCL was assumed to consist of a large number of periods forming a perfectly periodic cascade with N bound or quasibound states assigned to each period. The latter is justified by excellent localization properties of the confining potential in QCLs. Hence, the space and energy shift invariance of the potential enforce the same type of translation symmetry on the solutions of the Schrödinger equation, i.e., if the $\Psi(z,E)$ is a solution of the eigenvalue problem then $\Psi(z+L,E+\Delta V)$, where L is the length of the period, and ΔV is the potential drop across the period, will also be a solution as well. Furthermore, the scattering processes follow the same trend, i.e., the intraperiod scattering rate between equivalent states in any two periods is equal ($W_{i,j}=W_{i+kN,j+kN}$ $k=1,2,\ldots$.). Also, the shift invariance of the inter-period scattering between different periods requires that $W_{i-kN,j}=W_{i,j+kN}$ $k=1,2,\ldots$. In order to reduce the computational cost of calculating a large number of scattering rates, the model was embedded into a "tight-binding"-like picture, assuming that each period interacts with only a few of its nearest neighbors. Based on the symmetry rules in a cascade, a limited number of scattering rates between the states of a single period and its following P nearest neighbors needs to be calculated. Therefore, the total number of scattering rates is dependent on the number of chosen neighbors and bound states within the period state set and is equal to $N^2(2P+1)-N$. With the scattering rates known, a steady-state nonequilibrium electron distribution over quasidiscrete states of the injector/collector miniband and over states of the active region can be calculated by solving a system of rate equations given as

$$\frac{dn_i}{dt} = \sum_{j=1,j\neq i}^{N} n_j W_{j,i} - n_i \sum_{j=1,j\neq i}^{N} W_{i,j} + \sum_{k=1}^{P} \sum_{j=1,j\neq i}^{N} \{n_j[W_{j,i+kN} + W_{j+kN,i}] - n_i[W_{i+kN,j} + W_{i,j+kN}]\}. \quad (1)$$

Owing to the ultrafast nature of intersubband relaxation processes the system can be solved in the steady-state regime assuming $d/dt=0$. The system comprises of $N-1$ linearly independent equations completed with the particle conservation law, i.e., $\Sigma_i n_i = N_s$, where N_s is the total sheet electron density in each period. As the scattering rates are electron density dependent (i.e., usually averaged assuming Fermi-Dirac distributions over subbands), the solution of the system has to be found in the self-consistent manner, until the carrier distribution converges.[40,41] The physical meaning of the $i \neq j$ requirement in Eq. (1) is that intrasubband scattering processes are not influencing the electron population over states. However, such processes will later become relevant in the discussion of the electron heating in QCLs.

In order to simulate the influence of the injector doping density on the output characteristics of QCLs, the model was extended to include the effects of the dopant position and electron distribution on the electronic structure and dynamics. Commonly, the effective band profile including the electrostatic potential is calculated by iteratively solving the Schrödinger and the Poisson equations until the electronic structure converges. However, in the case of a highly nonequilibrium system such as a QCL (i.e., working in the high current injection regime), an electron distribution is not predefined, and in each step of the iterative procedure it has to be separately estimated. Hence, the electrostatic potential is dependent on the transport properties of the structure and both the Schrödinger and Poisson equations as well as the system of scattering rate equations [Eq. (1)] are intrinsically coupled. As a consequence, the convergence of both processes (self-self-consistency) is required for the accurate solution of the electron distribution over subbands. In the low bias regime applied across the QCL periods, i.e., in the lasing subthreshold, the carrier distribution over subbands becomes close to equilibrium and a common Fermi level across the structure can be assumed. In such a case, the electronic transport does not influence the electrostatic potential, and the scattering rate equations are decoupled from the Schrödinger-Poisson solver. Hence, the calculation becomes much simpler and is usually employed in the literature. However, the subthreshold regime does not reflect the real nature of the electronic transport in QCLs and cannot deliver the necessary insight into the lasing capabilities in case of a high doping level. In order to explore the influence of doping density on the above threshold QCL regime, the calculation in a fully self-self-consistent manner, described above, is required.

One should note that the electrostatic potential given as a solution of the Poisson equation is due to the quasiperiodic

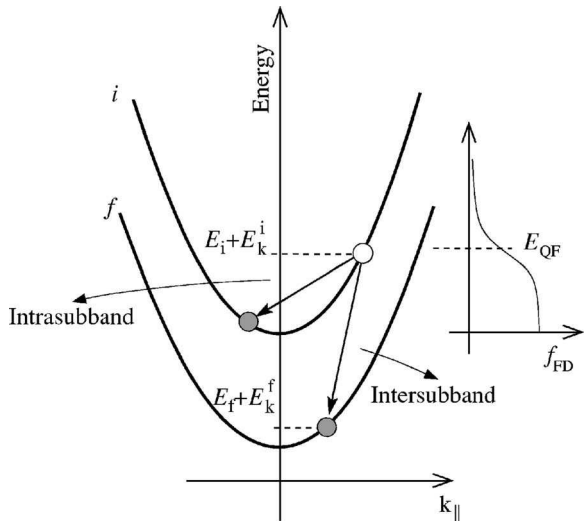

FIG. 1. Schematic illustration of the inter- and intrasubband scattering processes.

nature of the electron and donor distribution also periodic and needs to be found only for a single period and space shifted to map the whole structure.

A. Electron temperature

Owing to the various elastic or inelastic scattering interactions, electrons transfer their kinetic energy between subbands. A gain or loss of the total energy of the subband can be modeled in terms of the subband electron temperature, as previously done in the literature.[49,50] This assumes that the electron distribution in a subband is thermalized and thus, the extra kinetic energy of the electrons is quickly redistributed, and the distribution is rethermalized. The rate at which the kinetic energy is transferred between the subbands can be modeled in the rate equation framework, in a fairly similar manner as the electron densities over subbands. Hence, the electron in the ith state scattering into the fth state will result in a loss of energy in the ith state equal to its kinetic energy E_k^i. An increase of energy in the fth state based on the energy conservation law then reads

$$E_k^f = E_i - E_f + \delta E + E_k^i, \tag{2}$$

where δE is the energy of the scatterer, and $E_i - E_f$ is the "nonkinetic" energy gain/loss owing to the different energies of the subbands (Fig. 1). For elastic (electron-electron, impurity, etc.) and inelastic (electron-phonon) scattering interactions relevant in most QCLs, the energy of the scatterer can be written as

$$\delta E = \begin{cases} E_{\mathrm{LO}} & \text{for phonon absorption process} \\ -E_{\mathrm{LO}} & \text{for phonon emission processes} \\ 0 & \text{for elastic scattering processes,} \end{cases} \tag{3}$$

where E_{LO} is the LO-phonon energy. Two different energy rates corresponding to the $i \rightarrow f$ transition can be defined as $w_{i,f}^+$, representing the rate at which the energy of the fth state increases, and $w_{i,f}^-$, representing the rate at which the energy of the ith state decreases. Therefore, the equation defining the total energy rate of the subband reads

$$\frac{d\mathcal{E}_f}{dt} = \sum_i n_i w_{i,f}^+ - n_f \sum_i w_{f,i}^-. \tag{4}$$

The rate at which the energy of the final state increases ($w_{i,f}^+$) is equal to the product of the "incoming" kinetic energy [Eq. (2)] and the scattering rate corresponding to that energy state (i.e., in-plane wave vector) $W_{i,f}(E_k^i)$. The total rate can be found by averaging the product $\langle E_k^i W_{i,f}(E_k^i)\rangle$ over Fermi-Dirac distribution with respect to the subband temperature T_i and taking into account the Pauli exclusion principle as

$$w_{i,f}^+ = \frac{\int_0^\infty E_k^f W_{i,f}(E_k^i, T_i) f_{\mathrm{FD}}(E_{\mathrm{QF}}^i, T_i)[1 - f_{\mathrm{FD}}(E_{\mathrm{QF}}^f, T_f)] dE_k^i}{\int_0^\infty f_{\mathrm{FD}}(E_{\mathrm{QF}}^i, T_i) dE_k^i}, \tag{5}$$

where E_{QF}^i is the quasi-Fermi levels of the electron distribution on the ith state. By substituting the expression for E_k^i the latter reads

$$w_{i,f}^+ = (E_i - E_f + \delta E) W_{i,f} + \frac{\int_0^\infty E_k^i W_{i,f}(E_k^i, T_i) f_{\mathrm{FD}}(E_{\mathrm{QF}}^i, T_i)[1 - f_{\mathrm{FD}}(E_{\mathrm{QF}}^f, T_f)] dE_k^i}{\int_0^\infty f_{\mathrm{FD}}(E_{\mathrm{QF}}^i, T_i) dE_k^i}, \tag{6}$$

where $W_{i,f}$ is the average scattering rate. Similarly, the rate at which the energy of the ith state decreases ($w_{i,f}^-$) follows

$$w_{i,f}^- = \frac{\int_0^\infty E_k^i W_{i,f}(E_k^i, T_i) f_{\mathrm{FD}}(E_{\mathrm{QF}}^i, T_i)[1 - f_{\mathrm{FD}}(E_{\mathrm{QF}}^f, T_f)] dE_k^i}{\int_0^\infty f_{\mathrm{FD}}(E_{\mathrm{QF}}^i, T_i) dE_k^i}, \tag{7}$$

Hence, the $w_{i,f}^+$ and $w_{i,f}^-$ are related as

$$w_{i,f}^+ = (E_i - E_f + \delta E) W_{i,f} + w_{i,f}^-. \tag{8}$$

Although, not explicitly present in the particle rate equation, the intrasubband scattering ($w_{i,i}^+ = w_{i,i}^-$) has to be accounted for in the energy balance equation as the energy of an electron in the subband can change due to interaction with the lattice or due to $i,j \rightarrow i,j$-type electron-electron interaction, and thus the intrasubband scattering can be a mechanism of electron cooling or heating.

Hereafter, the balance equation is derived for the cascade in the tight-binding approximation. If the energy gain/loss rate is balanced, the total energy does not change in time, i.e., $d/dt = 0$, and thermalization of each subband can be characterized via a unique electron temperature (T_i). Hence, assuming P nearest neighbors, the Eq. (4) can be rewritten as

$$\frac{d\mathcal{E}_f}{dt} = 0 = \sum_{i=1}^{N} n_i w_{i,f}^+ - n_f \sum_{i=1}^{N} w_{f,i}^- + \sum_{k=1}^{P} \sum_{i=1}^{N} [n_i (w_{i,f+kN}^+ + w_{i+kN,f}^+) - n_f (w_{f+kN,i}^- + w_{f,i+kN}^-)], \tag{9}$$

where $w_{i,f}^+$ and $w_{i,f}^-$ are given by Eqs. (8) and (7). Equations (9) and (1) form a system of $2N$ nonlinear equations yielding N subband concentrations and N electron temperatures. However, recent experimental[51] and theoretical work[50] justified the use of a single (average) electron temperature (T_e) in the midinfrared QCLs. Furthermore, this considerably reduces the computational cost of solving of a nonlinear problem. Hence, the summing of the particular balance equations for each subband reads

$$\sum_{f=1}^{N}\frac{d\mathcal{E}_f}{dt}=0=\sum_{f=1}^{N}\sum_{i=1}^{N}n_i(E_i-E_f+\delta E)W_{i,f}+\underbrace{\sum_{f=1}^{N}\sum_{i=1}^{N}(n_i w^{-}_{i,f}-n_f w^{-}_{f,i})}_{=0}$$
$$+\sum_{f=1}^{N}\sum_{k=1}^{P}\sum_{i=1}^{N}\{n_i(E_i-E_{f+kN}+\delta E)W_{i,f+kN}+(E_{i+kN}-E_f+\delta E)W_{i+kN,f}\}$$
$$+\underbrace{\sum_{f=1}^{N}\sum_{k=1}^{P}\sum_{i=1}^{N}\{n_i[w^{-}_{i+kN,f}+w^{-}_{i,f+kN}]-n_f[w^{-}_{f+kN,i}+w^{-}_{f,i+kN}]\}}_{=0}, \tag{10}$$

where the physical meaning of the terms in the equation equal to zero, can be understood as the balance between the kinetic energy loss of the ith and the energy gain of the fth state owing to the $i\rightarrow f$ scattering. Hence, Eq. (10) does not comprise the integral terms. As the energy separation between the states of the different periods can be written in terms of the single period energies and the potential drop across the period (ΔV), i.e., $E_{i+kN}=E_i+k\Delta V$, the final form of the single temperature balance equation reads

$$\sum_{f=1}^{N}\sum_{i=1}^{N}n_i(E_i-E_f+\delta E)W_{i,f}+\sum_{f=1}^{N}\sum_{k=1}^{P}\sum_{i=1}^{N}n_i[(E_i-E_f-k\Delta V+\delta E)W_{i,f+kN}+(E_i-E_f+k\Delta V+\delta E)W_{i+kN,f}]=0. \tag{11}$$

The equation is coupled with the scattering rate equation [Eq. (1)], and as such, needs to be incorporated into the self-consistent procedure and evaluated in each iteration. That also adds on the complexity of the problem as the convergence of the electron temperature becomes a necessary requirement as well.

B. Output parameters

Having the electron distribution and temperature over subbands, physical observables such as current density, fractional injection, gain, and threshold current can be estimated. The current density in the QCL cascade is defined as[49]

$$J=\sum_{k=1}^{P}\sum_{i=1}^{N}\sum_{j=1}^{N}kn_i(W_{i,j+kN}-W_{i+kN,j}), \tag{12}$$

where the first term presents forward scattering into the states of the neighboring periods and the second term presents backscattering. The definition of the current density can also be used for estimating fractional injection as a ratio of the current injected into the upper laser level and the total current through the QCL.

In the two level approximation, the modal gain can be expressed as

$$G(\omega)=\frac{e^2\omega\pi}{cn_0\epsilon_0 L}\sum_{i=1}^{N}\sum_{f=1}^{N}n_i|z_{i,f}|^2\,\mathrm{sgn}(E_i-E_f)L(\omega,|E_i-E_f|)$$
$$+\sum_{k=1}^{P}\sum_{i=1}^{N}\sum_{f=1}^{N}n_i\{|z_{i,f+kN}|^2\,\mathrm{sgn}(E_i-E_f-k\Delta V)\times L(\omega,|E_i-E_f-k\Delta V|)+|z_{i+kN,f}|^2\,\mathrm{sgn}(E_i-E_f+k\Delta V)L(\omega,|E_i-E_f+k\Delta V|)\}, \tag{13}$$

where n_0 is the refractive index, L is the length of a period, $L(\cdot)$ is the Lorentzian assumed to describe well gain broadening, and "sgn" denotes the sign function of the argument. The modal gain is then equal to $G_M=g\Gamma$.

Having the current dependence of the modal gain, the threshold current can be evaluated based on a well-known formula: $G_M(J_{\mathrm{th}})=\alpha_W+\alpha_M$, where the α_M and α_W are the mirror and waveguide losses, respectively.

C. Electronic structure and scattering calculation

The subband energies and wave functions were calculated by solving the envelope function Schrödinger equation in an effective mass approximation with conduction band dispersion nonparabolicity taken into account via Kane's two-band model of the energy-dependent effective mass. The Schrödinger equation was solved for three full QCL periods. Clearly, the states confined mostly in the central period are calculated with better accuracy than states in other periods, owing to distant boundary conditions, and therefore these states have been taken to form a period state set. Based on the space and energy shift invariance, they were afterwards used to create the states of all other periods. The relevant scattering mechanisms that have been taken into account are based on electron-phonon, electron-electron, and electron-impurity interactions. The latter of which can be important at high doping levels. The scattering rates were calculated using Fermi's golden rule and averaged over the in-plane wave vector assuming Fermi-Dirac distributions over subbands. For calculating the electron-LO-phonon scattering, bulk phonon modes were assumed, which is widely used in the literature owing to a good agreement with the experiment for QCL structures.[34,38,40,47] Single subband screening of the

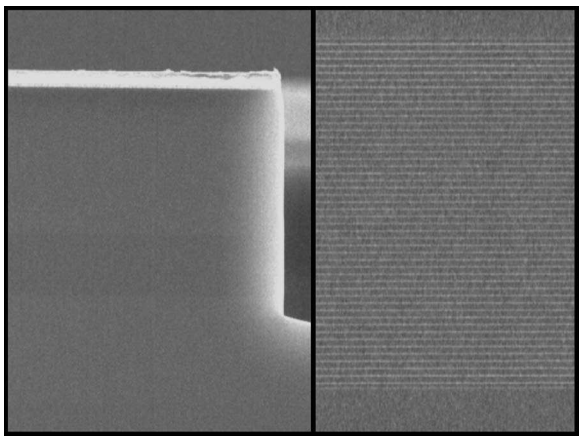

FIG. 2. SEM pictures of a cleaved facet of a processed ridge waveguide structure (left) and of the corresponding active region with 48 stages (right). The slightly darker region at the bottom of the ridge structure can be identified as the active region.

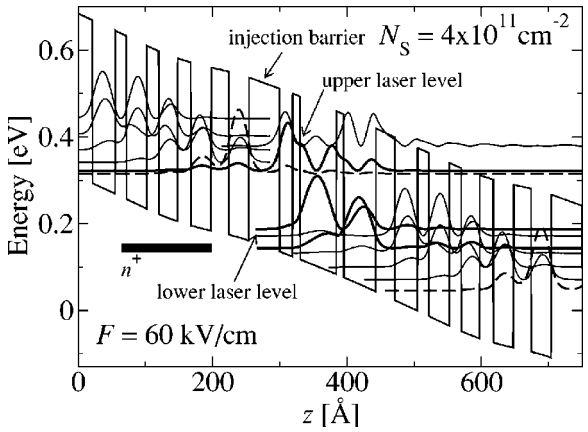

FIG. 3. A schematic diagram of a calculated self-self-consistent conduction band profile, quasibound energy levels, and wave functions squared for an injector-active region-collector segment of $GaAs/Al_{0.45}Ga_{0.55}As$ QCL for sheet carrier densities of 4.1×10^{11} cm^{-2} and an applied external electric field of 60 kV/cm at the 80 K. The laser levels are in bold, and the lowest injector state is in dashed lines. The doped region of the injector is also indicated.

electron-electron scattering was accounted for in the framework of the random phase approximation.[52] Based on a sample calculation, the acoustic phonon scattering was found to be a few orders of magnitude smaller than the LO-phonon scattering due to a large subband energy separation and a relatively high operating temperature and as such, assumed to be negligible.

III. DEVICE FABRICATION AND CHARACTERIZATION

For the experimental investigations, three wafers based on a three-quantum-well design[26] with doping levels of 4.1, 5.2, and 6.5×10^{11} cm^{-2} were grown in series with a solid source molecular beam epitaxy (MBE) system. The group III elements aluminium and gallium as well as the *n*-type dopant silicon were provided by conventional effusion cells (a dual filament cell was used for Ga). For arsenic a valved cracker cell was used in As_4 growth mode. The MBE system calibration and the layer quality confirmation were performed with high resolution x-ray diffraction and scanning electron microscopy. The layer structures were grown at a pyrometer temperature of 590 °C on the (001) plane of highly doped GaAs:Si substrates with a GaAs growth rate of 0.75 μm/h for the entire structure. The active regions comprise 48 cascaded stages embedded in a symmetrically grown plasmon enhanced waveguide[53,54] with 3.8 μm thick low doped (4×10^{16} cm^{-3}) and 1.2 μm highly doped (4×10^{18} cm^{-3}) GaAs layers. On the left of Fig. 2, a scanning electron microscopy (SEM) image of the laser facet is depicted. The slightly darker section at the bottom of the ridge can be identified as the active region, which is shown in a magnified SEM image on the right of Fig. 2.

Optimized arsenic fluxes were used for the growth of the active region layers and the waveguide layers.[45] The fluxes used for the waveguide [V/III beam equivalent pressure (BEP) ratio of 35] and the active region layers (V/III BEP ratio of 50 for GaAs layers, correspondingly less for AlGaAs layers) result in high-quality layers with smooth surfaces and low defect densities. Layer structures grown under these conditions exhibit threshold current densities of 2.9 kA/cm^2 (8.0 kA/cm^2) at 80 K (240 K) and maximum operation temperatures of around room temperature. In contrast, when the growth was performed with a constant III/V BEP ratio of 65 for both the waveguide and active region GaAs layers, we have observed increased threshold current densities of 5.1 kA/cm^2 (19 kA/cm^2) at 80 K (240 K) and the maximum operation temperature decreased to about 255 K.

In order to avoid current spreading and to achieve good lateral optical confinement, 18 to 34 μm wide ridge waveguide lasers were manufactured from the wafers by etching through the active region. For this purpose, the thinned wafers were processed by standard optical lithography and electron cyclotron resonance reactive ion etching in an Ar/C_{12} plasma. The bottom contacts (Au/Ge/Ni/Au) were deposited and alloyed, while the top contact (Cr/Pt/Au) was not alloyed and evaporated together with a thick Ni layer which served as the etch mask. Devices with 1 mm long cavities and uncoated facets were mounted episide up on copper heat sinks and wire bonded. For characterization, the QCLs were installed in a continuous flow helium cryostat and operated under pulsed conditions. All electro-optical measurements were made with 100 ns long pulses and repetition rates of about 500 Hz. The light output characteristics were determined with a fast mercury cadmium telluride (MCT) detector. Spectral characteristics were measured with a slow MCT detector in a Fourier transform infrared spectrometer setup in rapid scan mode.

IV. RESULTS AND DISCUSSION

The electronic and optical characteristics of the 45% Al$\sim$9 μm QCL design[26] have been investigated for the series of injector doping densities 4.1×10^{11}, 5.2×10^{11}, and 6.5×10^{11} cm^{-2}. Fully self-consistent calculations were performed for lattice temperatures of 80 and 240 K. The calculated band profile and wave functions squared for conventional doping of 4.1×10^{11} cm^{-2} at T=80 K are shown in Fig. 3. For the moderate doping conditions, the self-consistent band bending due to the specific electron distribu-

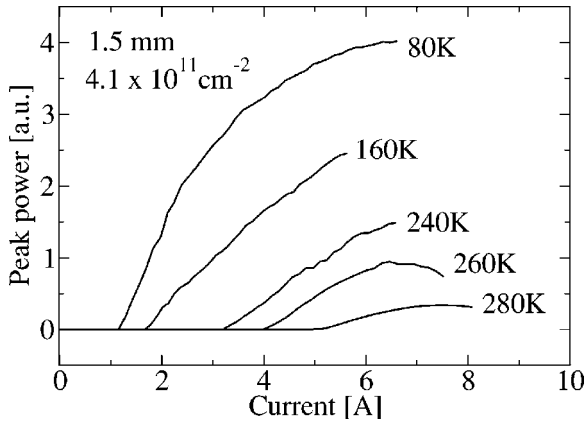

FIG. 4. Typical light output characteristics up to 280 K for a 1.5 mm long device with 4.1×10^{11} cm^{-2} injector sheet doping level.

tion is not very prominent, however, when higher doping is used, the band profile changes. That is especially important in the working regime around the resonant alignment between ground injector and upper laser levels.

As an example, the typical light output characteristics of a 1.5 mm long device with 4.1×10^{11} cm^{-2} injector doping level at several heat sink temperatures are shown in Fig. 4. As discussed in detail below, devices with an injector doping of 4.1×10^{11} cm^{-2} exhibit consistently lower threshold current densities compared to devices with higher doping concentrations.

The measured temperature dependence of the threshold current density of a corresponding 1 mm long device is given in Fig. 5. It is interesting to note that at 80 K, the threshold current density amounts to 2.9 kA/cm^2, which is a factor of 2 lower than that measured in devices with a sheet carrier concentration of 6.5×10^{11} cm^{-2}. The inset of Fig. 5 displays the typical Fabry-Perot emission spectrum of a device just above threshold taken at 80 K.

Figure 6 shows the theoretical (normal line and circles) and experimental (dashed line) field-current density characteristics for the analyzed injector doping densities at the lattice temperatures of 80 and 240 K. The calculated *I-V* curves have been shifted by a voltage drop across the waveguide and contacts, by fitting to experimental data found to be 2 V

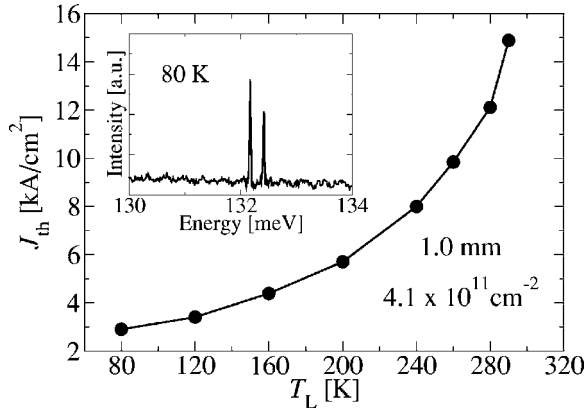

FIG. 5. Dependence of the threshold current density on temperature measured for the 1 mm long device. The inset shows a typical emission spectrum just above threshold taken at 80 K.

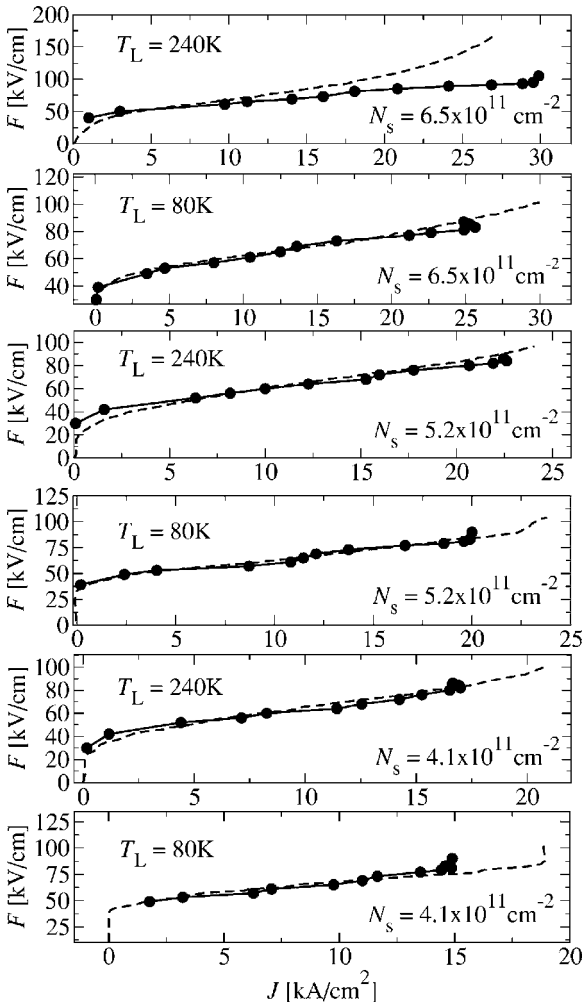

FIG. 6. Simulated current density-field characteristics for the three doping densities (4.1×10^{11}, 5.2×10^{11}, and 6.5×10^{11} cm^{-2}) at the lattice temperatures of 80 and 240 K (normal line and circles). The voltage drop across the waveguide and contacts of around ~2V was assumed. The measured current density-field characteristics are presented with dashed lines.

at 80 K and 2.6 V at 240 K. An excellent agreement, both quantitatively and qualitatively, between the simulation and the experimental measurements was found. There is an especially good agreement in the slope of the *I-V* curves, giving a good match for the structure's differential resistivity.

However, the theoretical maximal current density (just before the current saturation) is generally lower than measured. For example, in the case of the "4.1" device at 80 K it is around 14 kA/cm^2, which is somewhat lower than the measured value of 19 kA/cm^2. That could be explained with leakage mechanisms existing in the real QCL devices and not accounted for in the calculations. Furthermore, a certain discrepancy was observed between the calculated and measured *I-V* curves at higher fields for the injector doping of 6.5×10^{11} cm^{-2} at 240 K. In that particular case, the experimental measurement is showing a larger differential resistivity than expected, probably owing to imperfect contacts.

The fractional injection is calculated as a function of the energy spacing between the upper laser level and the lowest injector state (ΔE_l) and presented in Fig. 7 for different injector doping densities at 80 and 240 K. The bell-like shape of the fractional injection is observed for both temperatures,

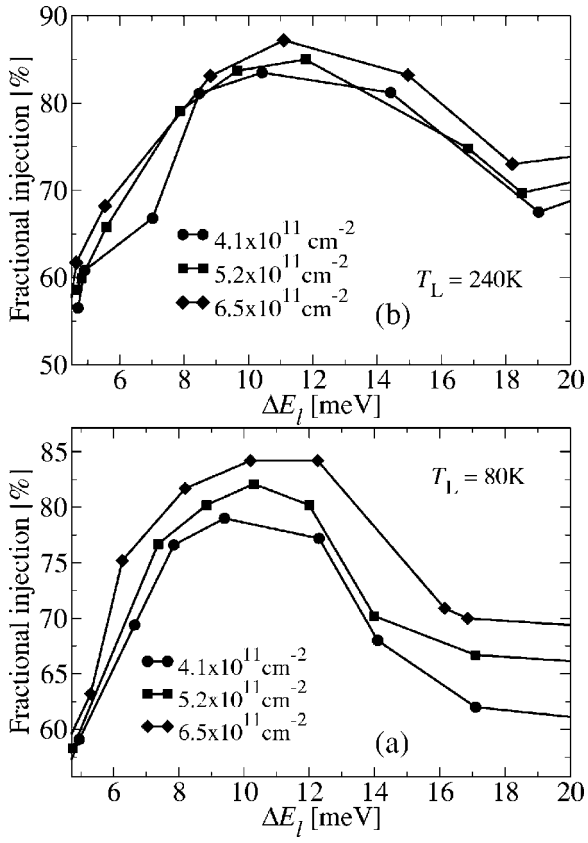

FIG. 7. Fractional injection as a function of the energy difference between the upper laser level and the lowest injector state calculated for the three doping densities of 4.1×10^{11} cm^{-2} (circles), 5.2×10^{11} cm^{-2} (squares), and 6.5×10^{11} cm^{-2} (diamonds) at the lattice temperatures of (a) 80 and (b) 240 K.

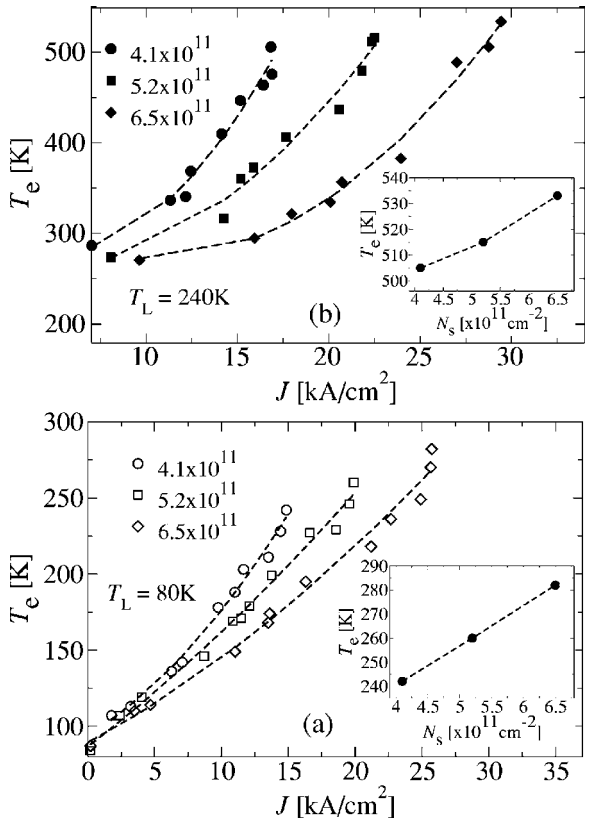

FIG. 8. Calculated electron temperature as a function of the current density for the three doping densities of 4.1×10^{11} cm^{-2} (circles), 5.2×10^{11} cm^{-2} (squares), and 6.5×10^{11} cm^{-2} (diamonds) at the lattice temperatures of (a) 80 and (b) 240 K. Quadratic fits are given by dashed lines. Insets: The maximal simulated electron temperature as a function of the injector doping density.

showing a maximum in the range of ΔE_l between 10 and 12 meV. In the range below 10 meV the fractional injection drops rapidly, due to an enhanced backfilling from the upper laser level into the lowest injector state in the conditions close to resonance. Moreover, as this occurs at higher electric fields, the parasitic current channels via higher injector states and a quasicontinuum exist, decreasing a fraction of the total current going through the upper laser level. An increase of the fractional injection with doping density was observed at 80 K, ranging from ~75% at 4.1×10^{11} cm^{-2} to ~85% at 6.5×10^{11} cm^{-2}. This is a consequence of enhanced injection from the lowest injector state into the upper laser level via electron-electron scattering in the higher doping regime. However, at 240 K the increase of the fractional injection with doping is not pronounced, as the scattering rates become less sensitive to the band filling at the higher temperatures.

The electron temperature in the single temperature approximation, calculated as a function of current density at 80 and 240 K, for different doping densities is presented in Fig. 8. The dependences are well fitted by a quadratic function (dashed lines). However, for the range of working current densities, the quadratic bowing is rather small, thus a linear functional form can be adopted[50] and characterized by a electron temperature-current coupling constant. For a fixed value of the current density, a decrease of the electron temperature with doping has been calculated. A more macroscopic explanation can be presented in terms of an effective decrease of input electrical power P_E, i.e., the same value of the current density at higher doping corresponds to the lower applied bias than in case of a lower doping (see Fig. 7). Also, the power per electron decreases as the number of electrons increases. Hence, for the same current density, the electrons in the QCL, in the higher doping regime, need to heat up less than for lower doping, in order to facilitate a LO-phonon emission and an efficient heat dissipation. This was confirmed by calculating the ratio between the relative increase in electron temperature and power of each individual electron $(T_e-T_L)/(P_E/N_s)$ which shows almost constant behavior for all doping levels. Consequently, the coupling constant drops with increased doping from 10.3 K/kA cm^{-2} at 4.1×10^{11} cm^{-2} to 7.1 K/kA cm^{-2} at 6.5×10^{11} cm^{-2} at 80 K and from 22.2 K/kA cm^{-2} at 4.1×10^{11} cm^{-2} to 14.2 K/kA cm^{-2} at 6.5×10^{11} cm^{-2} at 240 K. The value at 4.1×10^{11} cm^{-2} at 240 K is in excellent agreement with recently published experimental value of ~28 K/kA cm^{-2} determined from microprobe photoluminescence measurements,[51] but somewhat larger (~50%) than the first theoretical prediction reported earlier,[50] due to more scattering mechanisms taken into account in this calculation. The maximal value of the electron temperature, which corresponds to the current density just before saturation, is found to increase linearly with doping. The evaluated increase was around

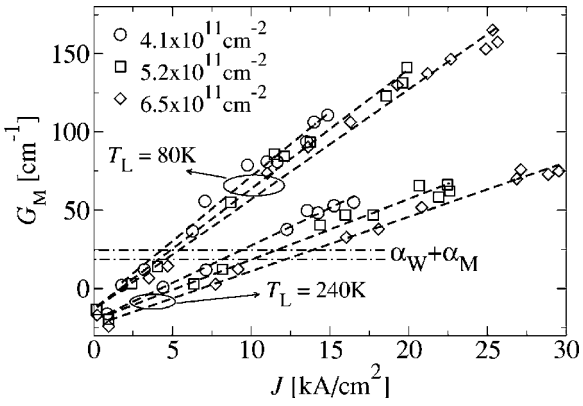

FIG. 9. Calculated modal gain for three injector doping densities at 80 and at 240 K. Dot-dashed lines represent the range of calculated total losses.

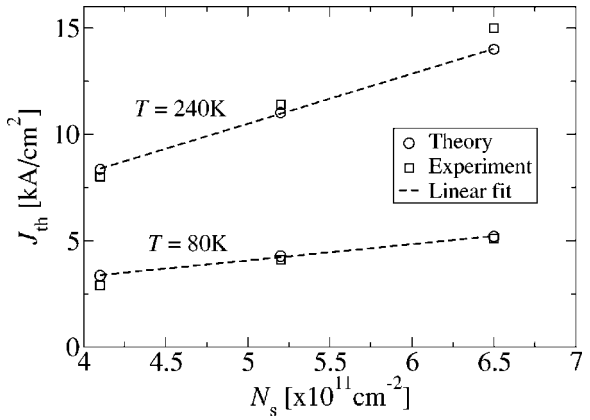

FIG. 10. Simulated threshold current density (circles) and corresponding experimental measurements (squares) as functions of the injector doping density at the temperatures of 80 and 240 K. The linear fits of theoretically obtained values are represented by dashed lines.

40 K (i.e. 17%) at 80 K in comparison with ~20 K (6%) at 240 K. The latter is due to reduced LO-phonon scattering sensitivity to doping density change at high temperatures.

The lasing performance of the QCLs has been theoretically investigated by calculating the modal gain as a function of the current density (Fig. 9). The waveguide parameters (losses α_W and confinement factor Γ) were calculated using the transfer matrix approach combined with the Drude model for the material parameters. Due to a greater number of periods in the QCL stack (48), the calculated confinement factor is slightly higher than in the original structure by Page *et al.*,[26] ranging between 0.37 for 4.1×10^{11} cm^{-2} to 0.34 for 6.5×10^{11} cm^{-2}. However, the estimated waveguide losses are quite similar and they are in range between $\alpha_W = (15-19)$ cm^{-1}, see dot-dashed lines in Fig. 9 where the mirror losses are assumed to be $\alpha_M \approx 6$ cm^{-1}. The full widths at half maximum (FWHM) of the electroluminescence line were taken[26] to be 12 meV at 80 K and 22 meV at 240 K and assumed to vary linearly by 1 meV in total in the range of examined doping densities. As expected, the gain exhibits quasilinear behavior and can be fitted by a linear function (Fig. 9) up to the current saturation. For both temperatures of 80 and 240 K, the slope of the gain (modal gain coefficient) decreases with an increase in doping. That is due to a changing interplay between the decrease in the lower laser level extraction efficiency (e.g., the lifetime at 80 K was reduced by 20%, from 0.34 to 0.28 ps in the examined range of doping), decrease of the mode confinement factor, and increase of the FWHM of the luminescence. The latter can especially deteriorate the laser performance at higher temperatures, where the gain margins are already quite narrow (see gain coefficient at 240 K in Fig. 9).

Knowing the modal gain dependence on the current density, a threshold current density (J_{th}) can be estimated. An excellent agreement with the experimental data was found, with an average discrepancy of around 5%, as shown in Fig. 10. The experimental value of the threshold current at 6.5×10^{11} cm^{-2} at 240 K was slightly higher than calculated, which is consistent with the previous discussion on the large differential resistivity exhibited by this particular QCL device. One should note that a simple threshold current estimate based on the unity injection approximation in the simple three-level QCL model, commonly used in literature,[13] does not exhibit a good agreement with the experiment. For both temperatures of 80 and 240 K, the threshold current density dependence on injector doping level can be characterized by a linear function of the form $J_{th}(N_s)\times(\mathrm{kA/cm^2}) = J_{th}(4.1) + \gamma(N_s - 4.1)$, where N_s is given in 10^{11} cm^{-2}. The calculated slope of the theoretical linear fit (dashed line on Fig. 10) was $\gamma \sim 0.77$ kA at 80 K and $\gamma \sim 2.35$ kA at 240 K, which is in a good agreement with the experimentally obtained $\gamma \sim 0.91$ kA at 80 K and $\gamma \sim 2.91$ kA at 240 K. The significantly larger γ can be associated with a considerably smaller gain coefficient at 240 K than at 80 K as well as a further drop due to an increased doping level. Having in mind the increase of the threshold current shown in Fig. 10 but also an increase of the saturation current with increased doping, one could consider the optimal value for the doping level for particular application purposes. Recently, it has been argued that in a particular QCL design "optimal" injector doping is suggested to be between 6×10^{11} and 8×10^{11} cm^{-2} in order to achieve significant gain and at the same time avoid the considerable increase in the threshold current.[55]

The theoretical model together with the experimental and numerical analysis presented above clearly show that doping density variations can play an important role in design and optimization of future high-performance QCL devices. This includes reduction of the threshold current and prolonged operation before saturation. Particularly, the linearized empirical formula for threshold current dependence on doping density can help in *ad hoc* optimization of GaAs devices in the midinfrared. Furthermore, insight into microscopic processes governing the electronic transport in QCLs such as electron heating and their connection to density of carriers can lead to increase in the dynamic range of lasing and deliver enhance flexibility in possible applications. Finally, the results presented in this paper can be applied and proved to be of considerable importance in the design and growth of long-wavelength and THz QCLs.

V. CONCLUSIONS

We have presented a detailed experimental and theoretical study of the impact of injector doping densities on the

output characteristic and carrier heating in GaAs/AlGaAs midinfrared QCLs. The employed theoretical model is based on a fully nonequilibrium Schrödinger-Poisson analysis of the coupled scattering rate and kinetic energy balance equations with all relevant electron-LO-phonon, electron-electron, and electron-ionized impurity interactions taken into account. Experimental analysis shows substantial reduction of the threshold current, particularly at higher temperature, when optimized arsenic fluxes were used during the growth procedure. The increase of the threshold current with doping level was characterized as quasilinear dependences with a very good agreement between calculations and experimental data.

ACKNOWLEDGMENTS

The authors would like to thank R. W. Kelsall, M. Giehler, and V. Spagnolo for useful discussions and M. Wagenbrenner and T. Demarczyk for expert technical assistance. Thanks go to J. Seufert of Nanoplus, Nanosystems and Technology GmbH for mounting the devices. The theoretical work in Leeds is partially supported by EPSRC(UK) and ORS(UK). Experimental work at Universität Würzburg was partially supported by the German Federal Ministry of Education and Research (project "Quankas").

[1] R. Kazarinov and R. Suris, Sov. Phys. Semicond. **5**, 707 (1971).
[2] J. Faist, F. Capasso, D. L. Sivco, C. Sirtori, A. L. Hutchinson, and A. Y. Cho, Science **264**, 553 (1994).
[3] C. Gmachl, A. Trediccuci, D. L. Sivco, A. L. Hutchinson, F. Capasso, and A. Y. Cho, Science **286**, 749 (1999).
[4] C. Gmachl, D. L. Sivco, J. N. Baillargeon, A. L. Hutchinson, F. Capasso, and A. Y. Cho, Appl. Phys. Lett. **79**, 572 (2001).
[5] C. Gmachl, D. L. Sivco, R. Colombelli, F. Capasso, and A. Y. Cho, Nature (London) **415**, 883 (2002).
[6] M. Beck, D. Hofstetter, T. Aellen, J. Faist, U. Oesterle, M. Ilegems, E. Gini, and H. Melchior, Science **295**, 301 (2001).
[7] A. Evans, J. S. Yu, J. David, L. Doris, K. Mi, S. Slivken, and M. Razeghi, Appl. Phys. Lett. **84**, 314 (2004).
[8] A. Evans, J. S. Yu, S. Slivken, and M. Razeghi, Appl. Phys. Lett. **85**, 2166 (2004).
[9] J.-Y. Bengloan, A. De Rossi, V. Ortiz, X. Marcadet, M. Calligaro, I. Maurin, and C. Sirtori, Appl. Phys. Lett. **84**, 2019 (2004).
[10] C. Gmachl, A. Belyanin, D. L. Sivco, M. L. Peabody, N. Owschimikow, A. M. Sergent, F. Capasso, and A. Y. Cho, IEEE J. Quantum Electron. **39**, 1345 (2003).
[11] T. S. Mosely, A. Belyanin, C. Gmachl, D. L. Sivco, M. L. Peabody, and A. Y. Cho, Opt. Express **12**, 2972 (2004).
[12] M. Troccoli, A. Belyanin, F. Capasso, E. Cubukcu, D. L. Sivco, and A. Cho, Nature (London) **433**, 845 (2005).
[13] C. Sirtori, P. Kruck, S. Barbieri, P. Collot, J. Nagle, M. Beck, J. Faist, and U. Oesterle, Appl. Phys. Lett. **73**, 3486 (1998).
[14] K. Ohtani and H. Ohno, Jpn. J. Appl. Phys., Part 2 **41**, L1279 (2002).
[15] K. Ohtani, K. Fujita, and H. Ohno, Jpn. J. Appl. Phys., Part 2 **43**, L879 (2004).
[16] R. Teissier *et al.*, Appl. Phys. Lett. **85**, 167 (2004).
[17] Q. Yang, C. Manz, W. Bronner, Ch. Mann, L. Kirste, K. Köhler, and J. Wagner, Appl. Phys. Lett. **86**, 131107 (2005).
[18] Q. Yang, C. Manz, W. Bronner, L. Kirste, K. Köhler, and J. Wagner, Appl. Phys. Lett. **86**, 131109 (2005).
[19] D. G. Revin, L. R. Wilson, E. A. Zibik, R. P. Green, J. W. Cockburn, M. J. Steer, R. J. Airey, and M. Hopkinson, Appl. Phys. Lett. **85**, 3992 (2004).
[20] D. Scalari, S. Blaser, J. Faist, H. Beere, E. Linfield, D. Ritchie, and G. Davies, Phys. Rev. Lett. **93**, 237403 (2004).
[21] R. Köhler *et al.*, Nature (London) **417**, 156 (2002).
[22] B. S. Williams, S. Kumar, H. Callebaut, Q. Hu, and J. L. Reno, Appl. Phys. Lett. **83**, 5142 (2003).
[23] S. Kumar, B. S. Williams, S. Kohen, Q. Hu, and J. L. Reno, Appl. Phys. Lett. **84**, 2494 (2004).
[24] S. Barbieri, J. Alton, H. E. Beere, E. H. Linfield, and D. A. Ritchie, Appl. Phys. Lett. **85**, 1674 (2004).
[25] S. Barbieri, C. Sirtori, H. Page, M. Stellmacher, and J. Nagle, Appl. Phys. Lett. **78**, 282 (2001).
[26] H. Page, C. Becker, A. Robertson, G. Glastre, V. Ortiz, and C. Sirtori, Appl. Phys. Lett. **78**, 3529 (2001).
[27] S. Anders, W. Schrenk, E. Gornik, and G. Strasser, Appl. Phys. Lett. **80**, 1864 (2002).
[28] C. Pflügl, W. Schrenk, S. Anders, G. Strasser, C. Becker, C. Sirtori, Y. Bonetti, and A. Muller, Appl. Phys. Lett. **83**, 4698 (2003).
[29] W. Schrenk, N. Finger, S. Gianordoli, E. Gornik, and G. Strasser, Appl. Phys. Lett. **77**, 3328 (2000).
[30] D. A. Carder, L. R. Wilson, R. P. Green, J. W. Cockburn, M. Hopkinson, M. J. Steer, R. Airey, and G. Hill, Appl. Phys. Lett. **82**, 3409 (2003).
[31] V. Ortiz, C. Becker, H. Page, and C. Sirtori, J. Cryst. Growth **251**, 701 (2003).
[32] H. Page, S. Dhillon, M. Calligaro, V. Ortiz, and C. Sirtori, Electron. Lett. **39**, 1053 (2003).
[33] H. Page, S. Dhillon, M. Calligaro, C. Becker, V. Ortiz, and C. Sirtori, IEEE J. Quantum Electron. **40**, 665 (2004).
[34] R. C. Iotti and F. Rossi, Phys. Rev. Lett. **87**, 146603 (2001).
[35] R. Köhler, R. C. Iotti, A. Tredicucci, and F. Rossi, Appl. Phys. Lett. **79**, 3920 (2001).
[36] H. Callebaut, S. Kumar, B. S. Williams, and Q. Hu, Appl. Phys. Lett. **84**, 645 (2004).
[37] O. Bonno, J.-L. Thobel, and F. Dessenne, J. Appl. Phys. **97**, 043702 (2005).
[38] S.-C. Lee and A. Wacker, Phys. Rev. B **66**, 245314 (2002).
[39] S.-C. Lee and A. Wacker, Appl. Phys. Lett. **83**, 2506 (2003).
[40] D. Indjin, P. Harrison, R. W. Kelsall, and Z. Ikonić, Appl. Phys. Lett. **81**, 400 (2002).
[41] V. D. Jovanović, D. Indjin, Z. Ikonić, and P. Harrison, Appl. Phys. Lett. **84**, 2995 (2004).
[42] M. Beck, International Workshop on Quantum Cascade Lasers, Seville, Spain, 4–8 January, 2004 (unpublished).
[43] G. Scarpa, P. Lugli, N. Ulbrich, G. Abstreiter, M.-C. Amann, M. Manenti, F. Comapgone, and A. Di Carlo, Semicond. Sci. Technol. **19**, S342 (2004).
[44] A. Straub, T. S. Mosley, C. Gmachl, R. Colombelli, M. Troccoli, F. Capasso, D. L. Sivco, and A. Y. Cho, Appl. Phys. Lett. **80**, 2845 (2002).
[45] S. Höfling, S. R. Kallweit, J. Seufert, J. Koeth, J. P. Reithmaier, and A. Forchel, J. Cryst. Growth **278**, 775 (2005).
[46] M. Giehler, R. Hey, H. Kostial, S. Cronenberg, T. Ohtsuka, L. Schrottke, and H. T. Grahn, Appl. Phys. Lett. **82**, 671 (2003).
[47] S.-C. Lee, M. Giehler, R. Hey, T. Ohtsuka, A. Wacker, and H. T. Grahn, Semicond. Sci. Technol. **19**, S45 (2004).
[48] M. Giehler, H. Kostial, R. Hey, and H. T. Grahn, J. Appl. Phys. **96**, 4755 (2004).
[49] Z. Ikonić, P. Harrison, and R. W. Kelsall, J. Appl. Phys. **96**, 269 (2004).
[50] P. Harrison, D. Indjin, and R. W. Kelsall, J. Appl. Phys. **92**, 6921 (2002).
[51] V. Spagnolo, G. Scamarcio, H. Page, and C. Sirtori, Appl. Phys. Lett. **84**, 3690 (2004).
[52] P. Harrison, *Quantum Wells, Wires and Dots: Theoretical and Computational Physics*, 2nd ed. (Wiley, Chichester, 2005).
[53] C. Sirtori, P. Kruck, S. Barbieri, H. Page, J. Nagle, M. Beck, J. Faist, and U. Oesterle, Appl. Phys. Lett. **75**, 3911 (1999).
[54] G. Scarpa, N. Ulbrich, A. Sigl, M. Bichler, D. Schuh, M.-C. Amann, and G. Abstreiter, Physica E (Amsterdam) **13**, 844 (2002).
[55] V. D. Jovanović *et al.*, Appl. Phys. Lett. **86**, 211117 (2005).